IET Generation, Transmission & Distribution

WILEY

The Institution of Engineering and Technology

ORIGINAL RESEARCH OPEN ACCESS

Robustness and Performance Analysis of a Current-Controlled Quasi-Stationary Electrical Model Virtual Synchronous Machine Using a Parameter-Dependent Operating Point

Christina Zuromski[1] | Francesco Giacomo Puricelli[2,3] | Jef Beerten[2,3] | Christian Becker[1]

[1]Hamburg University of Technology, Institute of Electrical Power and Energy Technology, Hamburg, Germany | [2]KU Leuven, Department of Electrical Engineering, Heverlee, Belgium | [3]EnergyVille, Etch, Genk, Belgium

Correspondence: Christina Zuromski (christina.zuromski@tuhh.de)

Received: 18 December 2025 | **Revised:** 11 March 2026 | **Accepted:** 24 March 2026

ABSTRACT

Ensuring stability in converter-dominated power systems requires voltage source converters to be robust under varying grid conditions and grid uncertainties such as short-circuit ratio variations. This paper analyzes the robustness of a grid-forming (GFM) current-controlled quasi-stationary electrical model virtual synchronous machine. We investigate the applicability of μ-analysis to systems incorporating GFM converters and demonstrate that operating point variations induced by parameter uncertainties must be explicitly considered. Due to the system's inherent nonlinearity, neglecting these variations can lead to misleading stability conclusions. To address the limitations of the μ-analysis, we introduce a robustness analysis method based on a parameter-dependent operating point and symbolic linearization, which enables efficient eigenvalue computation without repeated relinearization. Performance is additionally evaluated using sensitivity function analysis with respect to power reference tracking and angle disturbance rejection. The results show that appropriate control parameter selection improves robust stability under grid uncertainties by reducing undesired interactions.

1 | Introduction

As the penetration of converter-interfaced resources increases and the number of synchronous generators decreases, new challenges emerge in maintaining power system stability. In particular, the grid-forming (GFM) capabilities that are essential for stable operation, traditionally provided inherently by synchronous generators, must increasingly be supplied by power electronic converters. Consequently, various GFM control strategies for voltage source converters (VSCs) have been introduced [1]. Grid codes specify mandatory characteristics that are expected from the GFM converters, such as self-synchronization, damping of subsynchronous oscillations above 10 Hz, instantaneous active power changes for voltage angle jumps, and instantaneous reactive power changes for voltage amplitude jumps [2]. Furthermore, it is essential that the converter controls remain stable despite grid uncertainties. Ensuring such robustness under varying grid conditions is therefore a key requirement for future converter-dominated power systems. Such uncertainties in the grid model arise from unmodelled dynamics such as varying operational conditions, switching effects, measurement errors, uncertain control parameters, nearby VSCs, load variations, or also temperature effects [3–5]. Representing the grid as a Thévenin equivalent allows grid uncertainties to be characterized by variations in the grid impedance [3]. Assuming a constant X/R ratio, this leads to changes in the short-circuit ratio (SCR). Due to these uncertainties, it is essential to perform a robustness analysis of the converter controls to ensure that the converter remains stable

This is an open access article under the terms of the Creative Commons Attribution License, which permits use, distribution and reproduction in any medium, provided the original work is properly cited.

© 2026 The Author(s). *IET Generation, Transmission & Distribution* published by John Wiley & Sons Ltd on behalf of The Institution of Engineering and Technology.

under such conditions. A system is considered robustly stable when its controller can stabilize it regardless of any uncertainties within a defined set [6].

While classical eigenvalue analysis is widely used to assess small-signal stability, it examines stability at a single operating point. Thus, the robustness evaluation is limited to an interval in close proximity to the operating point. In such cases, approaches derived from robust control theory, such as the μ-analysis, may be more suitable. The μ-analysis is a robustness analysis based on the structured singular value and the small-gain theorem.

In this context, μ-analysis and robust control design based on singular value techniques have been applied to various contexts in power systems literature. For instance, [7] employs linearized models and μ-analysis for robust controller design in the context of FACTS devices. The designed controllers are subsequently applied to the nonlinear system for time-domain simulations. In [5], a μ-analysis of a linearized synchronverter is conducted using estimated input multiplicative uncertainties to account for parametric uncertainties and neglected system dynamics. The above studies have not systematically examined the potential inaccuracies resulting from neglecting nonlinearities in the control design or μ-analysis, a topic that is addressed in this paper. In contrast, [8] applies robustness investigations for multiplicative uncertainties of grid-following converters using singular values, considering the impact of nonlinearities of converter controls on the operating point. However, it is assumed that the nonlinearities are not affected by the uncertainty, and therefore the uncertainties have no impact on the operating point.

As stated in [9], the robust stability analysis and robust control design using the structured singular value are defined for linear systems. Thus, applying them to nonlinear systems is only valid if uncertainties have a sufficiently small impact on the system operating point.

Despite the contributions of the aforementioned papers, they either did not investigate the inaccuracies arising from linearization in robust control design and robust analysis or assumed that uncertainties have no impact on the operating point. Our work addresses this gap. We show that neglecting nonlinearities that significantly influence the operating point can lead to incorrect robustness conclusions when applying μ-analysis that is based on a linearization around a single operating point to converters under grid uncertainties. This is achieved by a comparative analysis of the results obtained from eigenvalue analyses and the μ-analysis, as well as by investigating a formulation of the μ-analysis that incorporates the impact of uncertainties on the operating point.

Consequently, a robustness analysis framework is required that explicitly incorporates the influence of parameter uncertainties on the operating point and overcomes the identified limitation of the μ-analysis. The main contribution of this paper is such a framework, in which the operating point is determined as a function of system parameters based on load-flow and algebraic equations. This subsequently enables the symbolic linearization of the nonlinear power system, such that nonlinearities of both system and converter control parameters on the operating point can be considered. Determining the operating point as a function of parameters requires greater effort than calculating a single operating point. However, the symbolically linearized state-space model avoids the main drawback of classical eigenvalue analyses with parameter sweeps, such as those in [10–12]: the need to recompute the operating point and relinearize the system for every parameter change. This recomputation and relinearization is also performed in [3], which compares the robustness of virtual impedance structures of virtual synchronous machines (VSMs) and their parametrization against grid impedance uncertainties rather than introducing a new stability analysis approach. Instead, the method proposed in this paper directly incorporates operating point variations resulting from parameter uncertainties into the linearized model. Thus, rapid eigenvalue analysis can be performed over a wide range of parameters and operating conditions without repeated operating point recalculation and system relinearization. Consequently, the influence of uncertain parameters on system stability can be assessed in a structured and computationally efficient manner, allowing robust stability limits to be systematically identified.

In addition to robust stability assessment, we also assess performance using sensitivity function analyses. While sensitivity functions are commonly applied in controller design, their potential for evaluating system performance, particularly power reference tracking and angle disturbance rejection, has not been widely adopted.

This paper examines the robust stability and performance of a GFM current-controlled quasi-stationary electrical model (CC-QSEM) VSM [13] and evaluates the feasibility and suitability of different analysis strategies for this purpose. The CC-QSEM approach is based on the quasi-stationary approximation of the synchronous machine and represents a preferred option for current-controlled VSM implementations compared to dynamic electrical model-based realizations [13]. The outer control structure follows the commonly adopted VSM concept, while the inner CC-QSEM realization enables straightforward implementation of current limitation in practical applications. Given that a weak grid interfaced with a CC-QSEM-based VSM is prone to instabilities [3], we evaluate the robustness and performance of a CC-QSEM VSM under SCR uncertainties, which reflect different AC grid conditions.

The remainder of this paper is structured as follows: Section 2 presents the theoretical basics, including μ-analysis, stability, and performance analysis. Section 3 describes the system model and its dynamics, including the GFM CC-QSEM VSM control. In Section 4, the proposed approach for calculating parameter-dependent operating points and performing symbolic linearization is presented. The applicability of μ-analysis to converter-dominated systems is examined in Section 5. Section 6 provides a detailed robustness stability, and performance analysis using parameter-dependent operating points and symbolically linearized system matrix. Finally, Section 7 concludes with key findings and recommendations for control parameter selection to enhance robustness against grid uncertainties.

17518695, 2026, 1, Downloaded from https://ietresearch.onlinelibrary.wiley.com/doi/10.1049/gtd2.70291 by Technische Universität Hamburg Universitätsbibliothek, Wiley Online Library on [16/04/2026]. See the Terms and Conditions (https://onlinelibrary.wiley.com/terms-and-conditions) on Wiley Online Library for rules of use; OA articles are governed by the applicable Creative Commons License

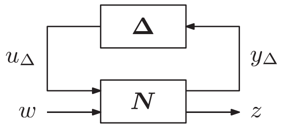

FIGURE 1 | $\boldsymbol{N\Delta}$-structure of the uncertain system.

2 | Theoretical Background

This section gives the theoretical background on the μ-analysis, small-signal stability analysis using eigenvalues and participation factors, as well as on the applied performance analysis.

2.1 | μ-Analysis

The μ-analysis is an effective approach to analyze the robustness of a linear time-invariant system with structured uncertainties. While this section provides the necessary background to understand the μ-analysis approach, a more elaborate presentation of this theory can be found in [6, 9, 14].

Singular values σ_i

$$\sigma_i(\boldsymbol{M}) = \sqrt{\lambda_i(\boldsymbol{M}\boldsymbol{M}^H)}, \tag{1}$$

similarly to eigenvalues λ_i, characterize properties of an arbitrary $l \times m$ matrix $\boldsymbol{M}$ [14]. While for single input single output (SISO) systems, the magnitude $|G(j\omega)| = f(\omega)$ can be used for analysis purposes, the singular values $\sigma_i\,(G(j\omega)) = f(\omega)$ are equivalently applicable for multiple input multiple output (MIMO) systems. The largest singular value

$$\overline{\sigma}(\boldsymbol{M}) = \sqrt{\lambda_{\max}(\boldsymbol{M}\boldsymbol{M}^H)} \tag{2}$$

is the largest gain of the MIMO system for the input $u(\omega)$ at the frequency ω. Those singular values enable robust stability analysis of systems with uncertainties. For this purpose, the system is represented in a $\boldsymbol{N\Delta}$-structure (see Figure 1), where the uncertainty is extracted into a normalized uncertainty matrix $\boldsymbol{\Delta}(s)$ [14]. The corresponding transfer function $F = z/w$ is the upper linear fractional transformation (LFT)

$$F = F_u(\boldsymbol{N}, \boldsymbol{\Delta}) := \boldsymbol{N}_{22} + \boldsymbol{N}_{21}\Delta(I - \boldsymbol{N}_{11}\boldsymbol{\Delta})^{-1}\boldsymbol{N}_{12}. \tag{3}$$

Variable $\boldsymbol{\Delta}$ is called the structured uncertainty matrix if it is in block diagonal form

$$\boldsymbol{\Delta} = \mathrm{diag}[\delta_1, \dots, \delta_k, \Delta_{k+1}, \dots, \Delta_n]. \tag{4}$$

δ_i is a real or complex scalar, and Δ_i is a complex matrix. This is valid for parametric uncertainties, as used in this paper, that are in the form of $p_j = p_{j,0}(1 + p_{\mathrm{p_j}}\delta_{\mathrm{p_j}})$ with $p_{j,0}$ denoting the nominal parameter value, $p_{\mathrm{p_j}}$ the weighting element, and $\delta_{\mathrm{p_j}}$ the normalized bounded uncertainty with $|\delta_{\mathrm{p_j}}| \leq 1$. If unstructured uncertainties occur, as in the case of a perturbed system $G_p(s) = G_0(s)\,(I + \Delta_m(s))$ with nominal system G_0 and multiplicative input uncertainties Δ_m, then the uncertainty matrix $\boldsymbol{\Delta}$ is non-diagonal and can be fully occupied [9]. In the latter case of unstructured uncertainties, the small gain theorem is necessary and sufficient to prove robust stability [6, 9]. For parametric uncertainties that are analyzed in this paper, the small-gain theorem is a sufficient but not necessary stability condition, and it is very conservative. Instead, a structured singular value quantifying the robustness of a system regarding the structured uncertainties is applied to obtain a necessary and sufficient stability condition, called μ-analysis: Based on the small-gain theorem, the $\boldsymbol{N\Delta}$-structure in Figure 1 is robustly stable for structured uncertainties if

$$\det(I - \boldsymbol{N}\Delta) \neq 0 \quad \forall\, \omega,\ \forall\, \Delta \tag{5}$$

holds [9]. The definition for the structured singular value of $\boldsymbol{N}$ with respect to $\boldsymbol{\Delta}$ follows [6, 9, 14]:

$$\mu_\Delta(\boldsymbol{N}) := \begin{cases} \dfrac{1}{\min_{\Delta \mathrm{in} \Delta}\{\overline{\sigma}(\Delta)\}}, \text{ if } \det(I - \boldsymbol{N}\Delta) = 0 \\ 0, \text{ if } \det(I - \boldsymbol{N}\Delta) \neq 0\ \forall\, \Delta \in \boldsymbol{\Delta} \end{cases}. \tag{6}$$

Thus, the closed loop system $F_u(\boldsymbol{N}, \boldsymbol{\Delta})$ is robust stable if the nominal loop $F_u(\boldsymbol{N}, 0)$ is stable and if

$$\mu_\Delta(\boldsymbol{N}) < 1\ \forall\, \omega. \tag{7}$$

This μ-analysis is applied in this paper to the CC-QSEM VSM with parametric uncertainties.

2.2 | Stability Analysis

State-space analysis is a widely used method for assessing the small-signal stability of power systems. Beyond determining system stability, this approach facilitates the identification of instabilities and reveals dynamic interactions within the system. A nonlinear power system can be described by

$$\dot{\boldsymbol{x}} = \boldsymbol{f}(\boldsymbol{x}, \boldsymbol{u}) \tag{8a}$$

$$\boldsymbol{y} = \boldsymbol{g}(\boldsymbol{x}, \boldsymbol{u}) \tag{8b}$$

with $\boldsymbol{f} = [f_1, f_2, \dots, f_n]^{\intercal}$ and $\boldsymbol{g} = [g_1, g_2, \dots, g_r]^{\intercal}$. Subsequently, a linear time-invariant state-space representation can be obtained by linearizing the system (8b) around an operating point:

$$\Delta\dot{\boldsymbol{x}} = \boldsymbol{A}\Delta\boldsymbol{x} + \boldsymbol{B}\Delta\boldsymbol{u}, \tag{9a}$$

$$\Delta\boldsymbol{y} = \boldsymbol{C}\Delta\boldsymbol{x} + \boldsymbol{D}\Delta\boldsymbol{u}, \tag{9b}$$

where $\Delta\boldsymbol{x} \in \mathbb{R}^{n\times1}$, $\Delta\boldsymbol{u} \in \mathbb{R}^{m\times1}$, and $\Delta\boldsymbol{y} \in \mathbb{R}^{r\times1}$ are the state-, input-, and output-vector, respectively. The stability of the linearized system is assessed by analyzing the eigenvalues λ_i of the state matrix $\boldsymbol{A}$, which are obtained by solving the characteristic equation

$$\chi = \det(\boldsymbol{A} - \lambda\boldsymbol{I}) = 0. \tag{10}$$

If the computed eigenvalues fulfill $\mathcal{R}e\{\lambda_i\} < 0,\ \ \forall\ i = 1, \dots, n$, then the linearized system is asymptotically stable at the considered operating point.

17518695, 2026, 1, Downloaded from https://ietresearch.onlinelibrary.wiley.com/doi/10.1049/gtd2.70291 by Technische Universität Hamburg Universitätsbibliothek, Wiley Online Library on [16/04/2026]. See the Terms and Conditions (https://onlinelibrary.wiley.com/terms-and-conditions) on Wiley Online Library for rules of use; OA articles are governed by the applicable Creative Commons License

Participation factors, defined as $\pi_{k,i} = w_{i,k} \cdot v_{k,i}$, are computed using the corresponding left ($\boldsymbol{w_i}$) and right ($\boldsymbol{v_i}$) eigenvectors associated with each eigenvalue. These factors quantify the contribution of the k-th state variable to the i-th mode of the system [15]. When multiple state variables exhibit significant participation in the same mode, this indicates dynamic interactions among those states. In this study, participation factors are normalized with respect to the highest value for each mode, such that a value of 1 represents maximum participation and a value of 0 indicates no contribution.

2.3 | Performance Analysis

Sensitivity functions $S(j\omega)$ and complementary sensitivity functions $T(j\omega)$ are suitable for evaluating performance characteristics of control systems as well as for designing control structures [6, 9, 14]. They are defined by

$$S(j\omega) = \frac{1}{1 + G_o(j\omega)}, \tag{11}$$

and

$$T(j\omega) = \frac{G_o(j\omega)}{1 + G_o(j\omega)}, \tag{12}$$

where $G_o(j\omega) = K(j\omega) \cdot G(j\omega)$ represents the open loop of a classical feedback control system with controller $K(j\omega)$ and system transfer function $G(j\omega)$. In general, there are three important requirements for a closed control loop: good tracking performance, effective disturbance suppression, and efficient noise rejection [9]. While the first two are met if $|S(j\omega)|$ is small $\forall\omega$, the last is fulfilled if $|T(j\omega)|$ is small $\forall\omega$. Since $T(j\omega) + S(j\omega) = 1$, either the sensitivity $S(j\omega)$ or the complementary sensitivity $T(j\omega)$ can be small, but not both. As disturbances and reference tracking take place in the low-frequency range and noise is a high-frequency event, the following practical requirements are derived from the above theoretical ones:

$$|S(j\omega)| \ll 1, \text{ for small } \omega, \text{ and} \tag{13}$$

$$|T(j\omega)| \ll 1, \text{ for large } \omega. \tag{14}$$

One application of sensitivity and complementary sensitivity functions can be found in the mixed sensitivity problem within H_∞-design, where weighting functions are formulated to meet the performance requirements [9]. In [16] such weighting functions are specified for H_∞-control design for grid-connected converters to meet defined requirements regarding grid synchronization, power and voltage regulation, and admittance performances. One disadvantage of H_∞-controllers is that, in addition to the appropriate selection of weighting functions, the order of the controller is typically aligned with the order of the system [17]. This results in a high-order controller being required for larger systems. This work goes beyond the conventional use of sensitivity functions in controller design by employing them as performance evaluation metrics. Therefore, we apply sensitivity functions $S_{\Delta P}(j\omega)$ characterizing the active power reference tracking performance and $S_{\theta_{\mathrm{vsc}}}(j\omega)$ evaluating the angle disturbance rejection, as these two properties represent fundamental performance requirements of VSC control. According to Equation (13), both sensitivities should be small for low frequencies.

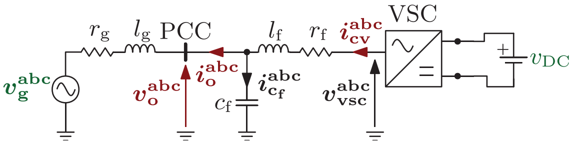

FIGURE 2 | System configuration.

3 | System Description and Converter Control

Figure 2 depicts the analyzed system, which comprises a VSC in GFM mode controlling the active and reactive power flow. The VSC is connected to an AC system through an LC filter. The terminal voltage and current of the converter are denoted as $\boldsymbol{v}_{\mathbf{vsc}}^{\mathbf{abc}}$ and $\boldsymbol{i}_{\mathbf{cv}}^{\mathbf{abc}}$, respectively. The resistor r_{f} represents the transformer resistance, while the inductance l_{f} accounts for the combined transformer and filter inductances. The current through the filter capacitor c_{f} is given by $\boldsymbol{i}_{\mathbf{cf}}^{\mathbf{abc}}$. At the point of common coupling (PCC), the current and voltage are indicated with $\boldsymbol{i}_{\mathbf{o}}^{\mathbf{abc}}$ and $\boldsymbol{v}_{\mathbf{o}}^{\mathbf{abc}}$, respectively. The AC system is represented using a Thévenin equivalent model with voltage $\boldsymbol{v}_{\mathbf{g}}^{\mathbf{abc}}$ and a constant angular frequency ω_{g}. The equivalent grid resistance r_{g} and inductance l_{g} are determined based on the short circuit level (SCL) at the PCC and the external grid reactance-to-resistance ratio k, as defined in [18]. The respective SCR is calculated with $\mathrm{SCR} = \mathrm{SCL}/S_{\mathrm{b}}$, where S_{b} is the base power. The voltage at the DC side of the converter v_{DC} is assumed to be constant.

To obtain a steady-state time-invariant representation, all system equations are transformed from a stationary abc to a rotating $dq0$ frame through a Park transformation $\boldsymbol{P}_{\theta}$. The variable θ represents the angle between the stationary reference frame a vector and the rotating direct axis d and it is obtained by integrating the dq frame rotational speed ω. In the selected Park transformation, the d-axis leads the q-axis by $\pi/2$ [19].

The grid and the converter dq variables are each defined in their own reference frame rotating at the grid angular frequency ω_{g} and the VSC synchronization angular frequency ω_{vsc}, respectively. To correctly connect the AC system with the converter variables in dq components, the dq interconnection variables must be defined in the same rotating reference frame. The AC system dq frame rotating at ω_{g} is selected as the global reference frame. Therefore, the interconnection variables in the converter reference frame must be rotated to the AC system (global) reference frame to ensure a consistent mathematical representation. This transformation represents a purely mathematical coordinate rotation and does not affect the physical transient behaviour of the system. The rotation matrix $\boldsymbol{R}_{\mathbf{c}\to\mathbf{g}}$ rotates the dq variables from a local $\boldsymbol{x}_{\mathbf{c}}^{\mathbf{dq}}$ to the global reference frame $\boldsymbol{x}^{\mathbf{dq}}$ by the angle $\Delta\theta_{\mathrm{vsc}}$

$$\underbrace{\begin{bmatrix} x^{\mathrm{d}} \\ x^{\mathrm{q}} \end{bmatrix}}_{\boldsymbol{x}^{\mathbf{dq}}} = \underbrace{\begin{bmatrix} \cos(\Delta\theta_{\mathrm{vsc}}) & \sin(\Delta\theta_{\mathrm{vsc}}) \\ -\sin(\Delta\theta_{\mathrm{vsc}}) & \cos(\Delta\theta_{\mathrm{vsc}}) \end{bmatrix}}_{\boldsymbol{R}_{\mathbf{c}\to\mathbf{g}}} \underbrace{\begin{bmatrix} x_{\mathrm{c}}^{\mathrm{d}} \\ x_{\mathrm{c}}^{\mathrm{q}} \end{bmatrix}}_{\boldsymbol{x}_{\mathbf{c}}^{\mathbf{dq}}}. \tag{15}$$

17518695, 2026, 1, Downloaded from https://ietresearch.onlinelibrary.wiley.com/doi/10.1049/gtd2.70291 by Technische Universität Hamburg Universitätsbibliothek, Wiley Online Library on [16/04/2026]. See the Terms and Conditions (https://onlinelibrary.wiley.com/terms-and-conditions) on Wiley Online Library for rules of use; OA articles are governed by the applicable Creative Commons License

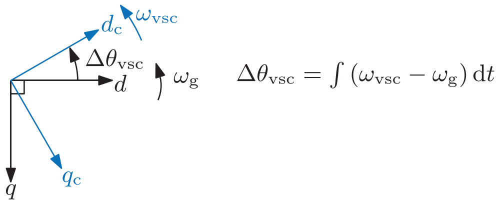

FIGURE 3 | Grid and converter rotating dq frames.

Figure 3 illustrates the global and converter rotating reference frames and the angle $\Delta\theta_{\mathrm{vsc}}$ between the two frames.

All the equations in the following subsections are defined in per unit (p.u.), and the system electrical and control parameters are included in Table A.1.

3.1 | Electric System Representation

This subsection outlines the differential equations of the electrical system in Figure 2, formulated in the global dq reference frame. These equations define the electrical state variables utilized in the state-space representation of the system through the following expressions

$$\frac{\mathrm{d}}{\mathrm{d}t}\boldsymbol{i}_{\mathrm{o}}^{\mathrm{dq}} = \frac{\omega_{\mathrm{b}}}{l_{\mathrm{g}}}\left(\boldsymbol{v}_{\mathrm{o}}^{\mathrm{dq}} - \boldsymbol{v}_{\mathrm{g}}^{\mathrm{dq}} - r_{\mathrm{g}} \cdot \boldsymbol{i}_{\mathrm{o}}^{\mathrm{dq}}\right) \mp \omega_{\mathrm{b}}\, \omega_{\mathrm{g,pu}}\, \boldsymbol{i}_{\mathrm{o}}^{\mathrm{qd}}, \tag{16a}$$

$$\frac{\mathrm{d}}{\mathrm{d}t}\boldsymbol{v}_{\mathrm{o}}^{\mathrm{dq}} = \frac{\omega_{\mathrm{b}}}{c_{\mathrm{f}}}\left(\boldsymbol{i}_{\mathrm{cv}}^{\mathrm{dq}} - \boldsymbol{i}_{\mathrm{o}}^{\mathrm{dq}}\right) \mp \omega_{\mathrm{b}}\, \omega_{\mathrm{g,pu}}\, \boldsymbol{v}_{\mathrm{o}}^{\mathrm{qd}}, \tag{16b}$$

$$\frac{\mathrm{d}}{\mathrm{d}t}\boldsymbol{i}_{\mathrm{cv}}^{\mathrm{dq}} = \frac{\omega_{\mathrm{b}}}{l_{\mathrm{f}}}\left(\boldsymbol{v}_{\mathrm{vsc}}^{\mathrm{dq}} - \boldsymbol{v}_{\mathrm{o}}^{\mathrm{dq}} - r_{\mathrm{f}} \cdot \boldsymbol{i}_{\mathrm{cv}}^{\mathrm{dq}}\right) \mp \omega_{\mathrm{b}}\, \omega_{\mathrm{g,pu}}\, \boldsymbol{i}_{\mathrm{cv}}^{\mathrm{qd}}. \tag{16c}$$

The presence of the base angular frequency ω_{b} derives from the per-unitization of the circuit equations, while $\omega_{\mathrm{g,pu}}$ indicates the p.u. grid angular frequency appearing in the cross-coupling term.

3.2 | Grid-Forming Converter Control

The VSC is controlled through a GFM VSM-based strategy, which is illustrated in Figure 4. The measured voltage $\boldsymbol{v}_{\mathrm{o}}^{\mathrm{abc}}$ and current $\boldsymbol{i}_{\mathrm{o}}^{\mathrm{abc}}$ at the PCC are transformed from abc to dq coordinates through the Park transformation $\boldsymbol{P}_{\theta}$ using the VSC synchronization angle θ_{vsc} (Figure 4a). The active p_{AC} and reactive q_{AC} powers, controlled by the VSC, are computed from the dq components of the PCC voltage $\boldsymbol{v}_{\mathrm{o,c}}^{\mathrm{dq}}$ and current $\boldsymbol{i}_{\mathrm{o,c}}^{\mathrm{dq}}$ with

$$p_{\mathrm{AC}} = v_{\mathrm{o,c}}^{\mathrm{d}} i_{\mathrm{o,c}}^{\mathrm{d}} + v_{\mathrm{o,c}}^{\mathrm{q}} i_{\mathrm{o,c}}^{\mathrm{q}}, \tag{17a}$$

$$q_{\mathrm{AC}} = v_{\mathrm{o,c}}^{\mathrm{d}} i_{\mathrm{o,c}}^{\mathrm{q}} - v_{\mathrm{o,c}}^{\mathrm{q}} i_{\mathrm{o,c}}^{\mathrm{d}}. \tag{17b}$$

Low pass filters (LPFs) are included in the active and reactive power measurements, and the filtered variables $p_{\mathrm{AC,f}}$ and $q_{\mathrm{AC,f}}$ are, respectively, obtained as shown in Figure 4b.

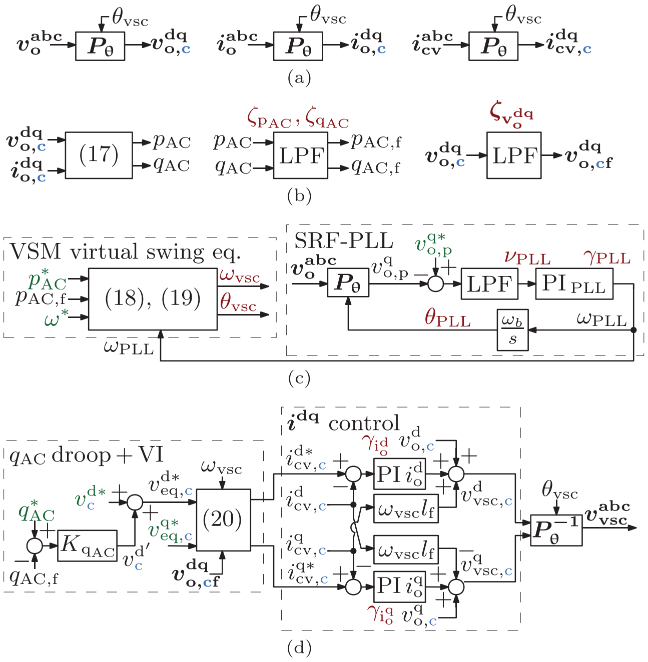

FIGURE 4 | GFM converter control architecture. (a) Park transformation. (b) Power calculation and LPFs. (c) VSM and SRF-PLL structure. (d) Reactive power droop, QSEM, and current control structure.

The synchronization angle θ_{vsc} used in the transformation $\boldsymbol{P}_{\theta}$ is obtained by integrating the per unit VSM angular frequency ω_{vsc}

$$\theta_{\mathrm{vsc}} = \omega_{\mathrm{b}} \int \omega_{\mathrm{vsc}}\, \mathrm{d}t, \tag{18}$$

where ω_{b} is the base angular frequency in rad/s. The variable ω_{vsc} is obtained through the VSM virtual swing equation

$$\begin{aligned}\frac{d\omega_{\mathrm{vsc}}}{dt} = \frac{1}{2H_{\mathrm{vsc}}}\big(&p_{\mathrm{AC}}^{*} - p_{\mathrm{AC,f}} - K_{\mathrm{d}}(\omega_{\mathrm{vsc}} - \omega_{\mathrm{PLL}}) + \\ &-K_{\omega}(\omega_{\mathrm{vsc}} - \omega^{*})\big).\end{aligned} \tag{19}$$

The VSM tunable coefficients are the inertia constant H_{vsc}, the damping coefficient K_{d}, and the droop coefficient K_{ω}. The other variables not previously defined represent the active power reference at the PCC p_{AC}^{*}, the PLL angular frequency ω_{PLL} used for damping purposes and detected by a synchronous reference frame phase-locked loop (SRF-PLL) [20], and the VSM angular frequency reference ω^{*}. A PLL is used to estimate the frequency used in the damping term, as this approach offers improved small-signal stability compared to alternative frequency estimation methods [21]. Figure 4c shows the control structure of the VSM and the SRF-PLL described above. The adopted VSM control strategy emulates the dynamics of a synchronous machine. The virtual swing equation establishes the coupling between active power imbalance and frequency dynamics in analogy to the classical motion swing equation. The damping coefficient K_{d} corresponds to mechanical damping, while the droop coefficient K_{ω} provides frequency support. In contrast to conventional synchronous machines, the inertia is not stored in a rotating mass but needs to be provided from the DC side, for example, with additional battery storage.

17518695, 2026, 1, Downloaded from https://ietresearch.onlinelibrary.wiley.com/doi/10.1049/gtd2.70291 by Technische Universitat Hamburg Universitatsbibliothek, Wiley Online Library on [16/04/2026]. See the Terms and Conditions (https://onlinelibrary.wiley.com/terms-and-conditions) on Wiley Online Library for rules of use; OA articles are governed by the applicable Creative Commons License

The voltage at the terminal of the converter is set by specifying a voltage reference $\boldsymbol{v}_{\mathrm{eq,c}}^{\mathrm{dq}*}$ in the input of the CC-QSEM virtual impedance (VI) [10] (Figure 4d). This name derives from the fact that the VSM virtual resistance r_{s} and inductance l_{s} are control variables and not physical components. Furthermore, the VI outputs current references based on an algebraic (i.e., quasi-stationary) assumption. Reactive power management is possible through a droop control with coefficient $K_{\mathrm{q_{AC}}}$; the output of the droop control modifies the value of $v_{\mathrm{eq,c}}^{\mathrm{d}*}$. The input references $v_{\mathrm{c}}^{\mathrm{d}*}$ and $v_{\mathrm{eq,c}}^{\mathrm{q}*}$ are set to 1 and 0, respectively. The expression for obtaining the current references for the current controller is

$$\boldsymbol{i}_{\mathbf{cv,c}}^{\mathbf{dq}*} = \frac{\boldsymbol{v}_{\mathbf{eq,c}}^{\mathbf{dq}*} - \boldsymbol{v}_{\mathbf{o,cf}}^{\mathbf{dq}}}{r_{\mathrm{s}} + j\omega_{\mathrm{vsc}} l_{\mathrm{s}}}, \tag{20}$$

with the low pass filtered voltage $\boldsymbol{v}_{\mathbf{o,cf}}^{\mathbf{dq}} = \frac{\omega_{\mathrm{vf}}}{s+\omega_{\mathrm{vf}}} \boldsymbol{v}_{\mathbf{o,c}}^{\mathbf{dq}}$. The current controller is an SRF PI-based control in dq frame with feed-forward voltages and cross-coupling terms. The output of the current controller $\boldsymbol{v}_{\mathrm{vsc,c}}^{\mathrm{dq}}$ is transformed from a dq to an abc frame through $\boldsymbol{P}_{\theta}^{-1}$ finding the voltage $\boldsymbol{v}_{\mathbf{vsc}}^{\mathbf{abc}}$ at the terminals of the VSC.

All the described PI controllers are tuned using the pole placement method [22], with a damping coefficient ξ of 0.7. The selected bandwidth $\omega_{\mathrm{bw,i}}$ varies for each i-th control loop and is specified in Table A.1.

3.3 | Resume of State and Input Vectors

The system state variables are highlighted in Figures 2 and 4 with a red font and are included in the state vector $\boldsymbol{x} \in \mathbb{R}^{17}$.

$$\begin{aligned} \boldsymbol{x} = \Big[& \boldsymbol{i}^{\mathrm{dq}^{\intercal}}{}_{\boldsymbol{o}}, \boldsymbol{v}_{o}^{\mathrm{dq}^{\intercal}}, \boldsymbol{i}_{cv}^{\mathrm{dq}^{\intercal}}, \theta_{\mathrm{vsc}}, \zeta_{\mathrm{q}_{AC}}, \zeta_{\mathrm{p}_{AC}}, \dots \\ & \dots \omega_{\mathrm{vsc}}, \nu_{\mathrm{PLL}}, \gamma_{\mathrm{PLL}}, \theta_{\mathrm{PLL}}, \boldsymbol{\zeta}^{\intercal}_{\mathrm{v}_{\boldsymbol{o}}^{\boldsymbol{dq}}}, \boldsymbol{\gamma}^{\intercal}_{\mathrm{i}_{o}^{dq}} \Big]^{\intercal}. \end{aligned} \tag{21}$$

The system inputs are indicated in Figures 2 and 4 with a green font and are resumed in the input vector $\boldsymbol{u} \in \mathbb{R}^{9}$

$$\boldsymbol{u} = \left[\boldsymbol{v}_{\mathbf{g}}^{\mathbf{dq}^{\intercal}}, v_{\mathrm{DC}}, p_{\mathrm{AC}}^{*}, \omega^{*}, q_{\mathrm{AC}}^{*}, v_{\mathrm{c}}^{\mathrm{d}*}, v_{\mathrm{eq,c}}^{\mathrm{q}*}, v_{\mathrm{o,p}}^{\mathrm{q}*} \right]^{\intercal}. \tag{22}$$

4 | Approach for Parameter-Dependent Operating Point Calculation and Symbolic Linearization

The computation of a parameter-dependent operating point allows the nonlinear influence of uncertain system parameters on the operating point to be captured explicitly. This formulation enables the symbolic linearization and the incorporation of operating point variations directly into the state-space model, thereby facilitating efficient robustness analysis of converter controls to grid uncertainties over a wide parameter range.

For low-order systems, as in [23, 24], the operating point can be computed entirely analytically and symbolically, yielding an explicit expression in terms of the system parameters. However, in this paper, the power system dynamics described in Section 3 involve complex nonlinear relationships in both electrical and control equations, as well as transformations between rotating $dq0$ frames. These complexities prevent an explicit symbolic solution of the system's differential equations presented in Section 3. To address this, we propose the following approach: first, the PCC voltage $\boldsymbol{v}_{\mathbf{o}}^{\mathbf{dq}}$, impacted by the grid uncertainties, is computed as a function of uncertain parameters using load flow equations. Then, using algebraic equations, all state variables at the operating point are determined as functions of these uncertain parameters. Subsequently, based on this operating point, the nonlinear system is symbolically linearized and results in a linear state-space model depending on the uncertain parameters.

4.1 | PCC Voltage Determination via Load Flow Equations

As the load flow equations assume the system to be steady-state at an operating point, voltages and currents can be expressed as phasors. The two variables to be calculated using the load flow equations are the angle $\varphi_{\mathrm{v_o}}$ and amplitude $\hat{v}_{\mathrm{o}}$ of the phasor

$$\underline{v}_{\mathrm{o}} = \hat{v}_{\mathrm{o}} \cdot e^{j\varphi_{\mathrm{v_o}}} \tag{23}$$

in order to subsequently determine $\boldsymbol{v}_{\mathbf{o}}^{\mathbf{dq}}$

$$v_{\mathrm{o}}^{\mathrm{d}} = \mathcal{Re}\{\underline{v}_{\mathrm{o}}\} \tag{24a}$$

$$v_{\mathrm{o}}^{\mathrm{q}} = -\mathcal{Im}\{\underline{v}_{\mathrm{o}}\}. \tag{24b}$$

A virtual internal voltage $\underline{e}$ can be defined as

$$\underline{e} = \underline{v}_{\mathrm{o}} + \underline{z}_{\mathrm{s}} \cdot \underbrace{(\underline{i}_{\mathrm{o}} + \underline{i}_{\mathrm{cf}})}_{\underline{i}_{\mathrm{cv}}}, \tag{25}$$

with

$$\begin{aligned} &\underline{z}_{\mathrm{g}} = r_{\mathrm{g}} + 1j \cdot l_{\mathrm{g}}, && z_{\mathrm{s}} = r_{\mathrm{s}} + 1j \cdot l_{\mathrm{s}}, && \underline{v}_{\mathrm{g}} = 1 \cdot e^{j0^{\circ}}, \\ &\underline{i}_{\mathrm{o}} = (\underline{v}_{\mathrm{o}} - \underline{v}_{\mathrm{g}})/\underline{z}_{\mathrm{g}}, && \underline{i}_{\mathrm{c_f}} = 1j \cdot c_{\mathrm{f}} \cdot \underline{v}_{\mathrm{o}}, && \underline{s}_{\mathrm{o}} = \underline{v}_{\mathrm{o}} \cdot \underline{i}_{\mathrm{o}}^{*}. \end{aligned} \tag{26}$$

Using the virtual internal voltage $\underline{e}$, the following two load flow equations, that consider the active and reactive power behaviour of the CC-QSEM VSM, can be formulated

$$0 = \mathcal{Re}\{\underline{s}_{\mathrm{o}}\} - p_{\mathrm{AC}}^{*} \tag{27a}$$

$$0 = v_{\mathrm{c}}^{\mathrm{d}*} - \mathrm{abs}\left(\underline{e}\right) + K_{\mathrm{q_{AC}}} \cdot \left(q_{\mathrm{AC}}^{*} - \mathcal{Im}\{\underline{s}_{\mathrm{o}}\}\right). \tag{27b}$$

Although the complexity has decreased compared to the entire system of differential equations (21), a symbolical solution of (27) is still not feasible. However, if all parameters are known, the load flow equations (27) can be solved numerically very quickly. This can be done using classical load-flow solution methods such as Newton-Raphson or, as done in this work, with `vpasolve` from MATLAB. Due to this rapid calculation

17518695, 2026, 1, Downloaded from https://ietresearch.onlinelibrary.wiley.com/doi/10.1049/gtd2.70291 by Technische Universität Hamburg Universitätsbibliothek, Wiley Online Library on [16/04/2026]. See the Terms and Conditions (https://onlinelibrary.wiley.com/terms-and-conditions) on Wiley Online Library for rules of use; OA articles are governed by the applicable Creative Commons License

for selected parameter values, a quick approximation of $\boldsymbol{v}_{\mathbf{o}}^{\mathbf{dq}}$ in dependence on parameters is possible using a polynomial fit. In case of two parameters p_1 and p_2, a 3rd order approximation is chosen to provide sufficient detail:

$$\begin{aligned} x &= f(p_1, p_2) \\ &= c_{00} + c_{10}p_1 + c_{01}p_2 + c_{20}p_1^2 + c_{11}p_1p_2 + c_{02}p_2^2 + \cdots \\ &\quad c_{30}p_1^3 + c_{21}p_1^2p_2 + c_{12}p_1p_2^2 + c_{03}p_2^3. \end{aligned} \tag{28}$$

Here, $c_{ij}, i, j = 0, \dots, 3$ are the polynomial coefficients, and x is $\boldsymbol{v}_{\mathbf{o}}^{\mathbf{d}}$ or $\boldsymbol{v}_{\mathbf{o}}^{\mathbf{q}}$, respectively.

4.2 | Operating Point Determination via Algebraic Equations

Based on the determined approximations $\boldsymbol{v}_{\mathbf{o}}^{\mathbf{dq}}(p_1, p_2)$, and (25), (26), as well as on the algebraic relations of the converter controls, the system states (21) at the operating point can be calculated as functions of the parameters p_1, p_2. B details the respective algebraic equations.

4.3 | Symbolic Linearization

A symbolic linearization of the nonlinear system around the calculated parameter-dependent operating point can be performed, resulting in a parameter-dependent state matrix $\boldsymbol{A}(p_1, p_2)$. Based on this state matrix, the eigenvalues for various parameter combinations p_1 and p_2 can subsequently be calculated. The influence of the parameters on the operating point is thereby inherently taken into account in the linearized model.

4.4 | Resume of Parameter-Dependent Operating Point

With the proposed approach—combining load flow calculations and the solution of algebraic equations—the operating point can be determined quickly and accurately as a function of the uncertain parameters p_1, p_2, despite the required approximations. The above equations further allow for a rapid assessment of whether a parameter affects the load-flow equations or the operating point.

The parameter-dependent operating point is particularly well-suited for the robustness analyses presented in this work. Linearizing the set of nonlinear differential equations describing the system dynamics makes it possible to capture nonlinear effects as well as the influence of parameter uncertainties on the operating point. The result is a symbolically linearized system with a system matrix $\boldsymbol{A}(p_1, p_2)$ depending on parameters p_1, p_2, which can then be used for robustness analysis via μ-analysis (Section 5.1) or eigenvalue analysis (Section 6). Note that these parameters p_1, p_2 can be whatever parameters of the system or control are considered in the analysis.

Initially, the method is primarily intended for the robustness assessment of a converter interfaced to an equivalent grid representation, where dominant uncertainties can be captured by a limited number of parameters. In general, the proposed formulation assumes a predefined and fixed set of uncertain parameters. While the method is not restricted to two parameters, an increasing number of uncertain variables increases the approximation effort and the complexity of result interpretation. Nevertheless, the load flow equation-based approximation of the PCC voltage remains applicable to moderately larger systems, as the load flow equations remain scalable and straightforward to implement. The subsequent computation of the state values at the operating point via algebraic equations remains unchanged.

5 | Applicability of μ-Analysis for Converter-Dominated Power Systems

Before applying the analysis method based on the parameter-dependent operating point and symbolic linearization proposed above, the applicability of the μ-analysis to converter-dominated power systems is investigated. The corresponding theoretical framework, including the LFT representation, is summarized in Section 2.1.

This section performs the μ-analysis for different SCR uncertainties and compares the results with the eigenvalues of the system in case of the uncertainty limits to verify the results we obtain. The SCR uncertainties, representing grid uncertainties, are parametric uncertainties, expressed in the form of

$$\mathrm{SCR} = \mathrm{SCR}_0(1 + p_{\mathrm{SCR}}\delta_{\mathrm{SCR}}) \tag{29}$$

with nominal value SCR_0, normalized bounded uncertainty $|\delta_{\mathrm{SCR}}| \leq 1$, and weighting element p_{SCR}. Thus, the matrix $\boldsymbol{\Delta}$ of the structured uncertainties is in a block diagonal form. The respective uncertainty limits for the eigenvalue analyses are calculated with $\mathrm{SCR} = \mathrm{SCR}_0(1 \pm p_{\mathrm{SCR}})$, since the worst-case scenario is considered.

Figure 5a shows the results of the μ-analysis for different parametric uncertainties with $p_{\mathrm{SCR}} = 0.1$, $p_{\mathrm{SCR}} = 0.25$, and $p_{\mathrm{SCR}} = 0.5$, which means that there can be a maximum of $\pm 10\%$, $\pm 25\%$, and $\pm 50\%$ deviation of the nominal SCR, which is chosen $\mathrm{SCR}_0 = 6$. With increasing uncertainty, the distance to the robustness limit of 1 becomes smaller, yet the structured singular value μ_Δ is lower than 1 for all frequencies. Thus, the results of the μ-analysis indicate that the VSM control is robust to changes in the SCR. However, this is not the case, as evidenced by the results of the eigenvalue analysis (see Figure 5b). For the eigenvalue determination, the operating point was recalculated considering the respective SCR value at the uncertainty boundary. In the considered case with nominal $\mathrm{SCR}_0 = 6$, the uncertainty levels of -50% and -25% correspond to reduced SCR values of 3 and 4.5, respectively. For these, the recomputed eigenvalues move to the right-half plane and thus lead to instability of the system despite $\mu < 1$.

The comparison of the μ-analysis and the eigenvalues demonstrates that the GFM converter is too nonlinear and that disturbances and uncertainties have a significant influence on the system's operating point, thus making the representation of

17518695, 2026, 1, Downloaded from https://ietresearch.onlinelibrary.wiley.com/doi/10.1049/gtd2.70291 by Technische Universität Hamburg Universitätsbibliothek, Wiley Online Library on [16/04/2026]. See the Terms and Conditions (https://onlinelibrary.wiley.com/terms-and-conditions) on Wiley Online Library for rules of use; OA articles are governed by the applicable Creative Commons License

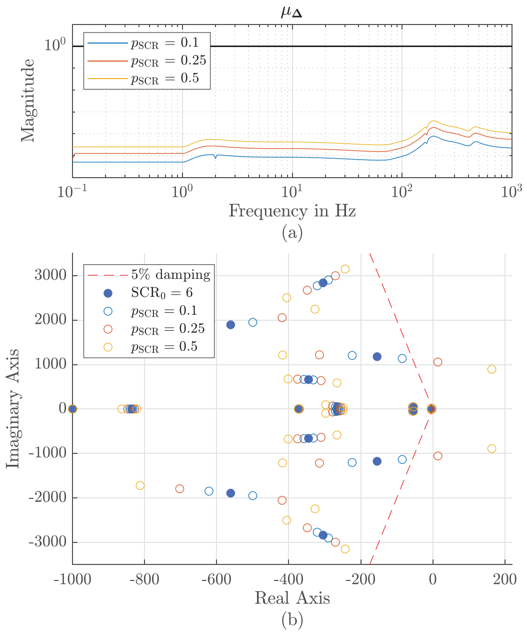

FIGURE 5 | Comparison of the structured singular value μ_Δ and corresponding eigenvalues for different uncertainty percentages of the SCR. (a) μ_Δ for ±10%, ±25%, and ±50% deviation of the nominal SCR. (b) Eigenvalues at the boundaries of the SCR uncertainties.

the system by a linearized system unsuitable for the successful application of the μ-analysis.

The application of unstructured input multiplicative uncertainties and the small gain theorem instead of parametric uncertainties and the μ-analysis, is also not useful. This is because the input multiplicative uncertainties are capable of representing uncertainties due to unknown dynamics by the formulation of weighting functions as upper estimates of the uncertainties. Consequently, these weighting functions are not well-suited for accurately representing parametric uncertainties, such as those related to the SCR and control parameters. Moreover, it is not possible to determine whether the input multiplicative uncertainties significantly affect the operating point, which means that applying μ-analysis in this context is inappropriate.

5.1 | μ-Analysis Considering Parameter-Dependent Operating Point

As demonstrated above, the μ-analysis is inapplicable to the linearized system due to the significant influence of nonlinearities and thus parametric uncertainties on the operating point. Consequently, the parameter-dependent operating point (introduced in Section 4) is applied for linearization in this section. This ensures that the influence of the parametric uncertainty of the SCR on the operating point is not neglected.

A major challenge with this approach is that non-rational functions, such as cos( ), or sin( ), which appear in the system dynamics due to the rotation matrix (15), must be calculated from uncertain parameters $p_j = p_{j,0}(1 + p_{\mathrm{p_j}}\delta_{\mathrm{p_j}})$. This calculation is undefined, as it would be unable to perform an exact LFT of the system, which is necessary to calculate the structured singular value. A possible workaround is to use Taylor approximations for the non-rational functions. However, this approach significantly increases the number of occurrences of the uncertain parameter in the system, linearized around the parameter-dependent operating point. As a result, it makes the μ-analysis extremely computationally demanding or even impossible to solve.

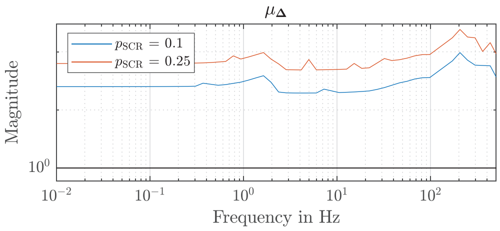

FIGURE 6 | Structured singular value μ_Δ for SCR uncertainties ±10% and ±25%, considering the impact of the uncertainties on the operating point and linearization.

Figure 6 shows the μ-analysis results using a parametric uncertainty for the SCR and first-order Taylor approximations used. Due to the applied approximations, robust stability is not indicated for 10% uncertainty, although it is present (see Figure 5b).

In summary, Sections 5 and 5.1 have shown significant limitations of the applicability of the μ-analysis. If parametric uncertainties significantly influence the operating point of a nonlinear system, μ-analysis based on a linearization at a single nominal operating point cannot guarantee reliable robustness conclusions for the underlying nonlinear system. On the other hand, incorporating parameter-dependent operating points into the μ-analysis framework introduces non-rational functions that require approximation, thereby increasing computational complexity and potentially leading to overly conservative results or unsolvability. Therefore, within the considered formulations, μ-analysis does not provide practically meaningful robustness guarantees for the studied system. These identified limitations emphasize the need for an alternative analysis method.

6 | Robust Stability Analysis of VSM Control Using Parameter-Dependent Operating Points

Due to the above limitations, this chapter performs a robust stability analysis using a parameter-dependent operating point according to Section 4. In the following, the parameters p_1 and p_2 correspond to the SCR, representing uncertain grid conditions, and to one varying control parameter, respectively.

By using the parameter-dependent operating point and resulting symbolically linearized system matrix $\boldsymbol{A}(p_1, p_2)$, stability can be assessed efficiently via eigenvalue analysis over a broad range of parameter variations, enabling the identification of robustness limits. Even with the approximations inherent to the parameter-dependent operating point, the approach can be considerably faster than repeatedly recalculating the operating point and re-linearizing the full system for each parameter variation and combination. In the latter case, for N operating points, recalculating the operating point by solving the system's differential equations and relinearization must be

17518695, 2026, 1, Downloaded from https://ietresearch.onlinelibrary.wiley.com/doi/10.1049/gtd2.70291 by Technische Universität Hamburg Universitätsbibliothek, Wiley Online Library on [16/04/2026]. See the Terms and Conditions (https://onlinelibrary.wiley.com/terms-and-conditions) on Wiley Online Library for rules of use; OA articles are governed by the applicable Creative Commons License

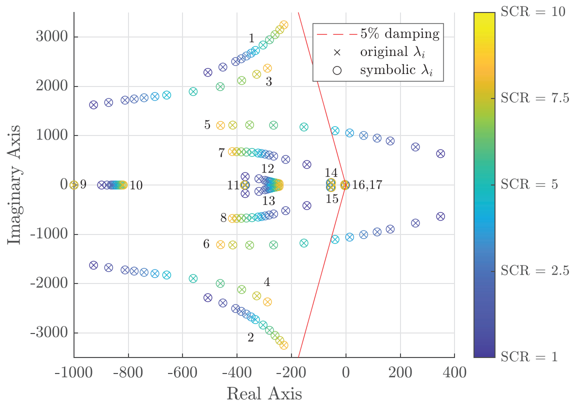

FIGURE 7 | Comparison of the eigenvalues, calculated by linearizing the system for each operating point and presented with ×, and eigenvalues using the parameter-dependent operating point marked with ∘.

performed N times, while the proposed approach requires a single parameter-dependent operating point calculation and symbolic linearization. Thus, the computational advantage of the proposed approach is especially evident for large-scale parameter sweeps with numerous operating points. For illustration, the computation of the parameter-dependent operating point and the subsequent symbolic linearization required about 1.7 s, whereas recomputation and relinearization for 100 operating points in the parameter range analyzed in Section 6.2 required approximately 75 s in total. This corresponds to a reduction in computation time of more than 95% using the proposed method. Although absolute values depend on the computational platform and parameter combinations, this example highlights the substantial efficiency gain for larger parameter sweeps. The calculation of the subsequent eigenvalues takes the same amount of time in both approaches.

By performing this stability analyses based on the parameter-dependent operating point, one can see how the control parameter value impacts the robustness of the system regarding grid uncertainties. Figure 7 illustrates the eigenvalues of the system that vary the most and become unstable for reduced SCR. Those eigenvalues are influenced by the current control and the QSEM VI states, as identified by the participation factors. For the QSEM VI, the low pass filter is critical for the stability [13], as well as the virtual inductance l_s has a major impact on the stability of the system [3]. Therefore, the robustness of both against SCR variations is analyzed in this section in Sections 6.2 and 6.3. Furthermore, the current control bandwidth that has a significant impact on the stability [25], is considered in Section 6.4.

6.1 | Validation

The comparison of the eigenvalues when relinearizing the system for each operating point and the eigenvalues computed using the proposed parameter-dependent operating point and subsequent symbolic linearized system according to Section 4 is presented in Figure 7 for uncertain SCRs. Since the eigenvalues match, it shows that the operating point depending on the parameter SCR was determined correctly through the proposed computation. The validity of the proposed approximation was tested for all the subsequent case studies, but these validations are not presented for conciseness. The close agreement of the eigenvalues further demonstrates that the approximation using the polynomial fit for the PCC voltage, explained in Section 4.1, does not noticeably affect the accuracy of the proposed approach. A quantitative error assessment further showed that the relative error between the approximated and the exact PCC voltage values over the considered SCR and parameter ranges is below 0.1 % for all case studies. This confirms that the third-order polynomial fit provides a sufficiently accurate representation for the stability analysis.

Note that in the subsequent stability analyses, the X/R ratio is assumed to be constant at a value of 10, representing a characteristic value typically found in transmission systems. This is a reasonable assumption given the predominantly inductive nature of transmission grids. Furthermore, the objective of this work is to demonstrate the proposed methodology through a representative application based on SCR variations, rather than to conduct an exhaustive study over all possible grid parameters. Accordingly, an uncertain SCR leads to an uncertain resistance r_g and inductance l_g of the Thévenin equivalent, both scaling linearly with the SCR due to the constant X/R ratio. Consequently, the SCR uncertainty of the grid can be represented by an uncertain r_g.

6.2 | Impact of QSEM Low-Pass Filter Bandwidth ω_{vf}

To assess the impact of the low-pass filter bandwidth ω_{vf} on system robustness against grid uncertainties, bandwidth values ranging from 30 rad/s to 600 rad/s are considered. Uncertainties of grid parameters are modelled using a variable SCR, which spans from 0.5 to 10. Figure 8 shows the stability limit of the system, depending on the SCR and the bandwidth ω_{vf}. It is observed that a higher filter bandwidth leads to decreased stability for weak grids. For example, bandwidths exceeding $\omega_{\mathrm{vf}} > 200$ rad/s require a strong grid, characterized by a SCR > 4.5, to maintain system stability.

In order to detect interactions that could compromise robust stability, the dominant eigenvalues close to the imaginary axis and sensitive to SCR uncertainties are analyzed through participation factor analysis. In this case, the complex conjugate pair of eigenvalues $\lambda_{5,6}$ is primarily critical for stability. The movement of these eigenvalues is presented in Figure 9 with increasing circles representing an increasing SCR, as also indicated by the direction

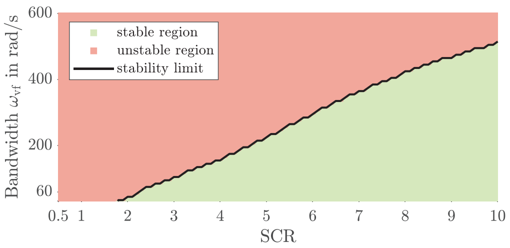

FIGURE 8 | Stability limit depending on the SCR and the bandwidth ω_{vf} of the low-pass filter of the QSEM with $l_s = 0.25$ p.u. and $\omega_{\mathrm{bw,cc}} = 2\pi \cdot 150$ rad/s.

17518695, 2026, 1, Downloaded from https://ietresearch.onlinelibrary.wiley.com/doi/10.1049/gtd2.70291 by Technische Universität Hamburg Universitätsbibliothek, Wiley Online Library on [16/04/2026]. See the Terms and Conditions (https://onlinelibrary.wiley.com/terms-and-conditions) on Wiley Online Library for rules of use; OA articles are governed by the applicable Creative Commons License

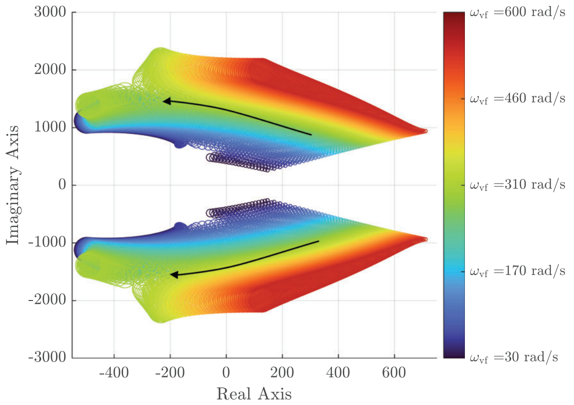

FIGURE 9 | Eigenvalues $\lambda_{5,6}$ depending on the SCR and the bandwidth ω_{vf} of the low-pass filter of the QSEM with $l_{\mathrm{s}} = 0.25$ p.u. and $\omega_{\mathrm{bw,cc}} = 2\pi \cdot 150$ rad/s. The arrows and increasing circles represent an increasing SCR from SCR = 0.5 to SCR = 10.

of the arrows. For smaller bandwidths with $\omega_{\mathrm{vf}} < 200$ rad/s, there is less displacement of $\lambda_{5,6}$. Thus, the sensitivity regarding uncertain grid conditions is smaller. Causes of instabilities in case of larger bandwidths can be identified using the participation factor plot in Figure A.1. For mode λ_5, the participation factors for the combinations of the different bandwidths and SCR values are presented. An explanation of how to read the participation factor plot is given in Figure A.4. The interactions between the QSEM filter states $\boldsymbol{\zeta}_{\mathbf{v}_{\mathrm{o}}^{\mathrm{dq}}}$, PCC voltage $\boldsymbol{v}_{\mathrm{o}}^{\mathbf{dq}}$, and current $i_{\mathrm{o}}^{\mathrm{q}}$ intensify with increasing bandwidth, occurring not only at low SCR values but also at higher SCR levels. Since Figures 8 and 9 show the same stability limit, the mentioned state variables are participating in the instability.

In contrast, the interactions between $i_{\mathrm{cv}}^{\mathrm{q}}$, $\zeta_{\mathrm{q_{AC}}}$, and $\gamma_{i_{\mathrm{o}}^{q}}$ increase for stable operating conditions, that is, at smaller bandwidths ω_{vf} and high SCR values. Hence, these interactions do not jeopardize stability but may even contribute positively. Moreover, the chosen PLL does not participate in the critical modes $\lambda_{5,6}$ and thus does not affect them. Hence, the PLL is not a limiting factor for stability, even in weak-grid scenarios (low SCR values), unlike in many cases presented in the literature.

In conclusion, smaller low-pass filter bandwidths of the QSEM are recommended to ensure stability and increase the robustness for uncertain grid conditions, represented by changing SCRs.

6.3 | Impact of QSEM Virtual Inductance l_{s}

The dependency of the stability on the virtual inductance l_{s} is clearly shown by the stability limit in Figure 10 with l_{s} values ranging from $= 0.1$ p.u. to 0.5 p.u.. Small l_{s} values lead to a significant decreasing stability area. Especially in weak grids, a larger l_{s} value is required to enable stability. Since the eigenvalues $\lambda_{5,6}$ are mainly responsible for instabilities due to uncertain grid conditions, their movement depending on the SCR and virtual inductance is presented in Figure 11. The enlarging circles and the direction of the arrow indicate the SCR increase. The higher the virtual inductance l_{s}, the less the eigenvalues $\lambda_{5,6}$ move with the changing SCR. Thus, the sensitivity to SCR uncertainties is lower, and therefore not only the stability but also the robustness to grid uncertainties is greater with larger l_{s}. Figure A.2 shows the corresponding participation factors for mode λ_5 that are equivalent to those of mode λ_6. The factors for all combinations for the range of SCR values from 0.5 to 10 and l_{s} from 0.1 p.u. up to 0.5 p.u. are given (see Figure A.4b). A reduction in virtual inductance l_{s} strengthens QSEM-induced interactions, such that the participation of the QSEM states in the critical eigenvalues $\lambda_{5,6}$ remains evident at small l_{s} values. In contrast, the interactions between $i_{\mathrm{cv}}^{\mathrm{q}}$ and current control state $\gamma_{i_{\mathrm{o}}^{q}}$ increase with increasing l_{s}, and therefore do not negatively affect stability. Both effects could already be identified in the previous stability analysis: QSEM-induced interactions generally have a negative impact on the robust stability, while those between the current controller and converter current are non-negative.

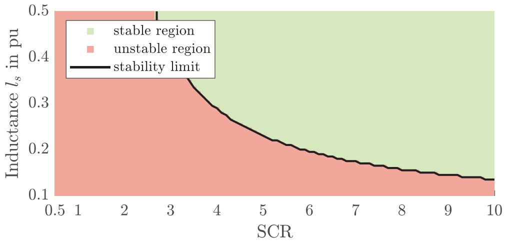

FIGURE 10 | Stability limit depending on the SCR and the virtual inductance l_{s} of the QSEM VI with $\omega_{\mathrm{vf}} = 200$ rad/s and $\omega_{\mathrm{bw,cc}} = 2\pi \cdot 150$ rad/s.

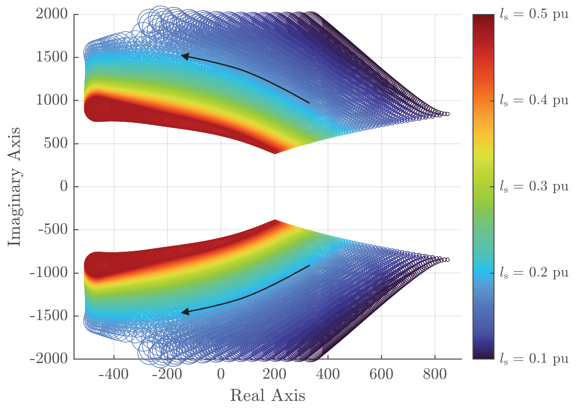

FIGURE 11 | Eigenvalues $\lambda_{5,6}$ depending on the SCR and the virtual inductance l_{s} of the QSEM VI with $\omega_{\mathrm{vf}} = 200$ rad/s and $\omega_{\mathrm{bw,cc}} = 2\pi \cdot 150$ rad/s. The arrows and increasing circles represent an increasing SCR from SCR = 0.5 to SCR = 10.

Thus, to ensure stability and robustness for uncertain grid conditions and avoid unstable interactions induced by the QSEM, larger values for l_{s} are recommended.

6.4 | Impact of Current Control Bandwidth $\omega_{\mathrm{bw,cc}}$

This subsection analyzes how the robustness of the converter to uncertain SCRs varies with different current control bandwidths, specifically for values of $\omega_{\mathrm{bw,cc}}$ from $50 \cdot 2\pi$ rad/s to $250 \cdot 2\pi$ rad/s. Figure 12 presents the stability limit depending on the SCR and current control bandwidth and shows that lower

17518695, 2026, 1, Downloaded from https://ietresearch.onlinelibrary.wiley.com/doi/10.1049/gtd2.70291 by Technische Universität Hamburg Universitätsbibliothek, Wiley Online Library on [16/04/2026]. See the Terms and Conditions (https://onlinelibrary.wiley.com/terms-and-conditions) on Wiley Online Library for rules of use; OA articles are governed by the applicable Creative Commons License

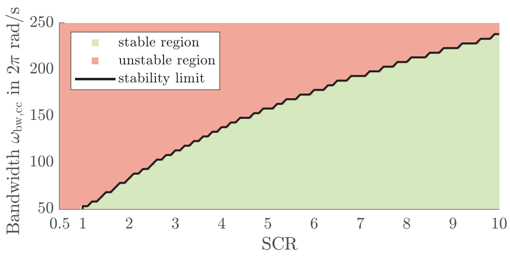

FIGURE 12 | Stability limit depending on the SCR and the current control bandwidth $\omega_{\mathrm{bw,cc}}$ with $l_{\mathrm{s}} = 0.25$ p.u. and $\omega_{\mathrm{vf}} = 200\,\mathrm{rad/s}$.

current control bandwidths result in a larger stability region for weak grids. This is primarily due to the reduced sensitivity of the critical eigenvalue $\lambda_{5,6}$ to changes in SCR for small $\omega_{\mathrm{bw,cc}}$ values, as illustrated in Figure 13. Consequently, system robustness increases significantly. This behavior can be further understood by examining the participation factors. Figure A.3 presents these factors for decreasing current control bandwidths and increasing SCRs, highlighting the underlying dynamics (see Figure A.4c). It can be seen that for the larger bandwidths, interactions between the QSEM states $\boldsymbol{\zeta}_{\mathrm{v}_{\mathrm{o}}^{dq}}$, which are the states of the measured PCC voltage, $\boldsymbol{v}_{\mathbf{o}}^{\mathbf{dq}}$, and $i_{\mathrm{o}}^{\mathrm{q}}$ occur, and increase for smaller SCR values. For small bandwidths, these critical interactions are not present, but those between the converter current $i_{\mathrm{cv}}^{\mathrm{q}}$, current control state $\gamma_{\mathrm{i}_{\mathrm{o}}^{q}}$, and $\zeta_{\mathrm{q_{AC}}}$ are present. The previous results explain why small current control bandwidths lead to better robustness against SCR variation. Moreover, the identified causes of positive and negative stability impacts align with those found in the previous two analyses in Sections 6.2 and 6.3.

6.5 | Performance Analysis

To further analyze the system's characteristics, a performance analysis considering sensitivity functions is performed. The sensitivity functions $S_{\Delta P}(j\omega)$ and $S_{\theta_{\mathrm{vsc}}}(j\omega)$ are similar to those used for the weighting function design in [16] and enable the evaluation of the converter's power reference tracking performance and angle disturbance rejection capability. The sensitivity functions are defined as

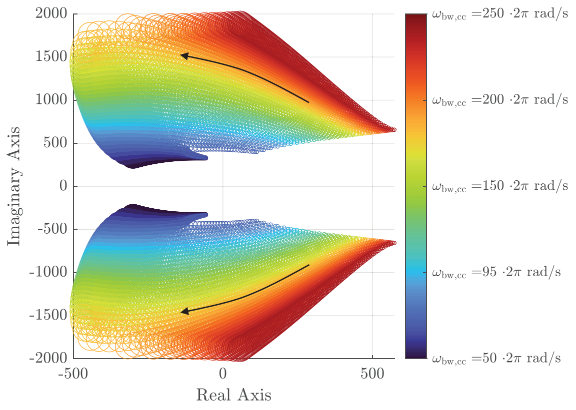

FIGURE 13 | Eigenvalues $\lambda_{5,6}$ depending on the SCR and the current control bandwidth $\omega_{\mathrm{bw,cc}}$ with $l_{\mathrm{s}} = 0.25$ p.u. and $\omega_{\mathrm{vf}} = 200\,\mathrm{rad/s}$. The arrows and increasing circles represent an increasing SCR from SCR = 0.5 to SCR = 10.

FIGURE 14 | Structure showing output and disturbance input of (a) sensitivity function $S_{\Delta P}$ and (b) sensitivity function $S_{\theta_{\mathrm{vsc}}}$.

$$S_{\Delta P}(j\omega) = \frac{z(j\omega)}{w(j\omega)} = \frac{\Delta P(j\omega)}{w_{p^*_{\mathrm{AC}}}(j\omega)} \tag{30}$$

$$S_{\theta_{\mathrm{vsc}}}(j\omega) = \frac{z(j\omega)}{w(j\omega)} = \frac{\theta_{\mathrm{vsc}}(j\omega)}{w_{\theta_{\mathrm{vsc}}}(j\omega)}. \tag{31}$$

$S_{\Delta P}(j\omega)$ characterizes the transfer behaviour from the disturbance $w = w_{p^*_{\mathrm{AC}}}$ to $z = \Delta P = p^*_{\mathrm{AC}} + w_{p^*_{\mathrm{AC}}} - \zeta_{p_{\mathrm{AC}}}$ (see Figure 14a). To achieve good tracking of the reference p^*_{AC}, the tracking error ΔP should be eliminated in lower frequencies, and thus,

$$|S_{\Delta P}(j\omega)| \ll 1 \text{ for small } \omega \tag{32}$$

must be fulfilled. If additionally

$$|S_{\theta_{\mathrm{vsc}}}(j\omega)| \ll 1 \text{ for small } \omega, \tag{33}$$

then there is good suppression of disturbance $w = w_{\theta_{\mathrm{vsc}}}$ to $z = \theta_{\mathrm{vsc}}$ (see Figure 14b). Thus, the controller has a good reaction performance to angle disturbances. In this context, the magnitude at low frequencies of the sensitivity function quantifies the disturbance rejection and reference tracking capability. The frequency at $-3\,\mathrm{dB}$ can be interpreted in the context of sensitivity functions as the frequency up to which disturbances are effectively suppressed.

The impact of the SCR (Figure 15) and the virtual inductance (Figure 16) l_{s} on the sensitivity curves is shown in the following.

Performance Analysis for Varying SCR: Figure 15 depicts the sensitivity functions $S_{\Delta P}(j\omega)$ and $S_{\theta_{\mathrm{vsc}}}(j\omega)$ and shows that in both performance analyses a good suppression of disturbances is achieved, since the sensitivity is small for low frequencies. In case of $S_{\theta_{\mathrm{vsc}}}(j\omega)$, the magnitudes at low frequencies indicate better angle disturbance suppression in case of a strong grid.

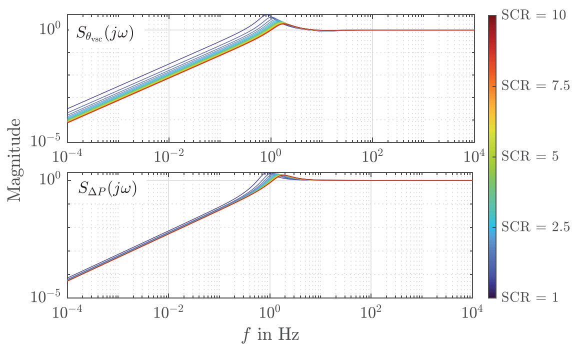

FIGURE 15 | Sensitivity $S_{\theta_{\mathrm{vsc}}}(j\omega)$ from disturbance $w = w_{\theta_{\mathrm{vsc}}}$ to $z = \theta_{\mathrm{vsc}}$ and Sensitivity $S_{\Delta P}(j\omega)$ from disturbance $w = w_{p^*_{\mathrm{AC}}}$ to $z = \Delta P = p^*_{\mathrm{AC}} + w_{p^*_{\mathrm{AC}}} - \zeta_{p_{\mathrm{AC}}}$.

17518695, 2026, 1, Downloaded from https://ietresearch.onlinelibrary.wiley.com/doi/10.1049/gtd2.70291 by Technische Universität Hamburg Universitätsbibliothek, Wiley Online Library on [16/04/2026]. See the Terms and Conditions (https://onlinelibrary.wiley.com/terms-and-conditions) on Wiley Online Library for rules of use; OA articles are governed by the applicable Creative Commons License

Moreover, under weak grid conditions, a higher magnitude peak occurs at around 1 Hz and reflects increased resonance in the frequency range of the dominant low-frequency VSM mode. Consequently, disturbances occurring near this frequency may be amplified under weak grid conditions. The exact magnitude and location of this peak depend on controller parameters such as virtual inertia constant, droop constant, and virtual impedance, as well as grid strength. From a practical perspective, adequate damping in this frequency range is therefore particularly relevant to meet grid code requirements and avoid unstable low-frequency oscillations.

This also occurs for $S_{\Delta P}(j\omega)$. Apart from that, the grid strength has negligible influence on the reference tracking performance, as shown in Figure 15.

The low pass filter bandwidth ω_{vf} and the current control bandwidth $\omega_{\mathrm{bw,cc}}$ have no significant impact on the shown sensitivity curves and thus are not presented for conciseness.

Performance Analysis for Varying SCR and Different l_s: Next to the SCR, the virtual inductance l_s has a significant impact on the sensitivity curves. Figures 16a and 16b show the sensitivities for a weak and a stronger grid scenario. In all cases, especially in the case of weak grids, a large virtual inductance of $l_s = 0.5$ p.u., leads to a smaller resonance peak. Thus, a higher l_s is not only advantageous in terms of stability and robustness (see Section 6.3), but also in terms of performance. The magnitudes at low frequencies indicate that the suppression of disturbances is better achieved with smaller l_s, however, the sensitivity at low frequencies remains sufficiently low even with higher l_s. Thus, good disturbance suppression can be guaranteed.

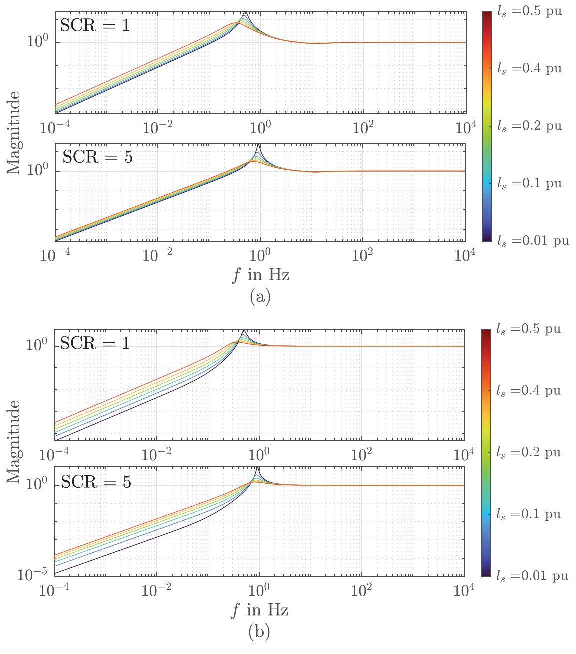

FIGURE 16 | Sensitivity curves depending on virtual inductance l_s for a weak grid scenario with SCR = 1 and a strong grid scenario with SCR = 5. (a) Sensitivity $S_{\theta_{\mathrm{vsc}}}(j\omega)$. (b) Sensitivity $S_{\Delta P}(j\omega)$.

Overall, it can be said that although there are differences in performance, the basic desired behavior specified by (32) and (33) to enable power reference tracking and angle disturbance is given for the analyzed parameters and grid strengths.

6.6 | Evaluation of Well and Poorly Tuned Parameter Combinations and Discussion

The robustness and performance analyses, presented in the previous subsections, highlight the critical role of QSEM-induced interactions in determining system stability under grid uncertainties. Specifically, the sensitivity of eigenvalues to SCR variations underscores the importance of parameter tuning. A larger virtual inductance l_s enhances robustness by reducing the system's sensitivity to SCR fluctuations, thereby mitigating instability risks in weak grid scenarios. Similarly, small low-pass filter ω_{vf} and current control bandwidths $\omega_{\mathrm{bw,cc}}$ effectively limit interactions that would otherwise make instabilities more likely.

However, selecting both bandwidths to be small simultaneously can introduce undesired additional coupling effects between the QSEM, PLL, and VSM, diminishing robustness. This can be seen in an exemplary scenario in Figure 17. The participation factors for mode 14 with an SCR = 1.75 are shown for the case where both bandwidths were chosen small with $\omega_{\mathrm{vf}} = 50\,\mathrm{rad/s}$, $\omega_{\mathrm{bw,cc}} = 2\pi \cdot 50\,\mathrm{rad/s}$ and for the case with $\omega_{\mathrm{vf}} = 200\,\mathrm{rad/s}$, $\omega_{\mathrm{bw,cc}} = 2\pi \cdot 50\,\mathrm{rad/s}$. In both cases, $l_s = 0.5$ p.u. When comparing the participation factors, it can be seen that the above-mentioned additional interactions occur in the case where both bandwidths are small. In the case of an SCR = 1, the system becomes unstable, which is not the case if the bandwidths $\omega_{\mathrm{vf}} = 200\,\mathrm{rad/s}$, $\omega_{\mathrm{bw,cc}} = 2\pi \cdot 50\,\mathrm{rad/s}$ were selected.

In the following, this latter combination is called well tuned parameter combination, which provides robust stability against SCR uncertainties with $0.75 \le \mathrm{SCR} \le 10$. In contrast, for a poorly tuned parameter combination with $\omega_{\mathrm{vf}} = 220\,\mathrm{rad/s}$, $\omega_{\mathrm{bw,cc}} = 2\pi \cdot 150\,\mathrm{rad/s}$, and $l_s = 0.3$ p.u., stability, especially robust stability, cannot be guaranteed. Figure 18 shows the results of nonlinear EMT time domain simulations for SCR changes that demonstrate this clearly: While the poorly tuned parameter set still provides robustness against increasing SCRs (Figure 18a), in the case of a decreasing SCR (Figure 18b), the system becomes unstable. This is consistent with the stability maps presented in Figures 8, 10, and 12. For the poorly tuned parameter combination, the critical SCR values predicted in the respective maps are significantly higher than for the well tuned case, indicating reduced robustness against decreasing SCR. This explains the improved stability for decreasing SCR values observed in the EMT simulations. The well tuned case further exhibits shorter settling times and less overshoot in Figure 18.

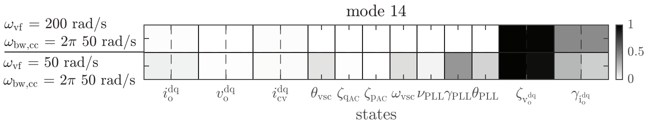

FIGURE 17 | Comparison of the participation factors for different bandwidth combinations of ω_{vf} and $\omega_{\mathrm{bw,cc}}$ for mode 14.

17518695, 2026, 1, Downloaded from https://ietresearch.onlinelibrary.wiley.com/doi/10.1049/gtd2.70291 by Technische Universität Hamburg Universitätsbibliothek, Wiley Online Library on [16/04/2026]. See the Terms and Conditions (https://onlinelibrary.wiley.com/terms-and-conditions) on Wiley Online Library for rules of use; OA articles are governed by the applicable Creative Commons License

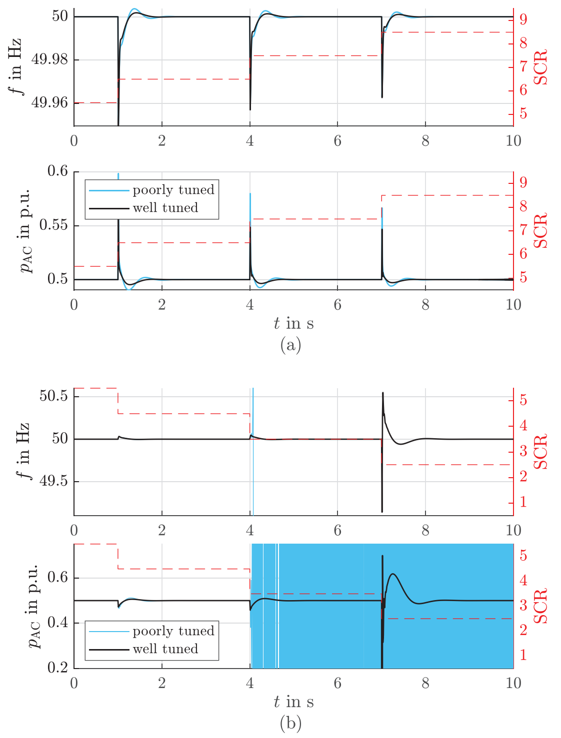

FIGURE 18 | Nonlinear EMT time domain simulations for a well and poorly tuned parameter combination. In case (a) for an increasing SCR and in (b) for a decreasing SCR.

7 | Conclusion

This paper identified key limitations of the structured singular value (μ) analysis for nonlinear converter-interfaced power systems when parametric uncertainties significantly influence the operating point. In such cases, linearization at a single operating point can lead to misleading stability margins in the μ-analysis. Moreover, incorporating parameter-dependent operating points into μ-analysis renders the method computationally demanding and prone to conservative results. These findings highlight the need for alternative robustness assessment methods better suited to nonlinear converter-dominated systems.

We therefore proposed an approach that determines parameter-dependent operating points from load flow and algebraic equations and enables symbolic linearization, allowing nonlinearities and parameter changes to be considered in the operating point. Furthermore, the equations make it straightforward to identify which parameters influence the operating point and which do not.

The proposed approach was applied to a CC-QSEM VSM under grid uncertainties to systematically analyze the impact of control parameters on robustness. The results show that instability is primarily driven by QSEM-induced interactions, while the interaction between the current controller and the converter current does not negatively impact system stability. Furthermore, appropriately tuned virtual inductance l_s, QSEM low-pass filter bandwidth ω_{vf}, and current control bandwidth $\omega_{\mathrm{bw,cc}}$ enhance both system stability and performance, enabling robust operation down to an SCR of 0.75 in the example shown. Sensitivity-function analysis confirms that stability-favorable parameter sets also support good power reference tracking and angle disturbance rejection.

Overall, the proposed method provides a systematic and computationally efficient robustness analysis framework that explicitly accounts for parameter-dependent operating point variations. It enables combined stability and performance evaluation and offers reliable robustness assessment of GFM control structures against grid uncertainties. The method is generally applicable to different VSC control structures and to nonlinear power systems in which the operating point depends on uncertain parameters. A relevant application could be improved control tuning during the design phase at manufacturers, where robust stability analysis can be assessed systematically. This enables manufacturers to enhance controller robustness to grid uncertainties.

Future work should apply the proposed approach to other GFM strategies and investigate robustness under different grid structures. The scalability aspects discussed in Section 4.4 should be considered in this context.

Author Contributions

Christina Zuromski: conceptualization, investigation, methodology, software, validation, writing – original draft. **Francesco Giacomo Puricelli**: conceptualization, methodology, writing – original draft. **Jef Beerten**: conceptualization, funding acquisition, supervision, writing – review & editing. **Christian Becker**: funding acquisition, supervision, writing – review & editing.

Acknowledgements

This work was supported by a fellowship of the German Academic Exchange Service (DAAD) and by the Belgian Energy Transition Fund, FOD Economy, project DIRECTIONS. The publishing fees are supported by Funding Programme Open Access Publishing of Hamburg University of Technology (TUHH).

Open access funding enabled and organized by Projekt DEAL.

Conflicts of Interest

The authors declare no conflicts of interest.

Data Availability Statement

The data that support the findings of this study are available from the corresponding author upon reasonable request.

References

1. R. Rosso, X. Wang, M. Liserre, X. Lu, and S. Engelken, “Grid-Forming Converters: Control Approaches, Grid-Synchronization, and Future Trends—A Review,” *IEEE Open Journal of Industry Applications* 2 (2021): 93–109, https://doi.org/10.1109/OJIA.2021.3074028.

2. VDE FNN, *Technische Anforderungen an Netzbildende Eigenschaften Inklusive der Bereitstellung von Momentanreserve / Technical Requirements for Grid-Forming Capabilities Including Provision of Inertia* (2025, version: 2.0), https://www.vde.com/de/fnn/aktuelles/netzbildende-eigenschaften.

3. T. Tutturen, J. A. Suul, and S. D’Arco, “Robust Choice of Virtual Impedance for Virtual Synchronous Machines Accounting for Grid Impedance Uncertainty,” in *2024 International Symposium on Power*

17518695, 2026, 1, Downloaded from https://ietresearch.onlinelibrary.wiley.com/doi/10.1049/gtd2.70291 by Technische Universitat Hamburg Universitatsbibliothek, Wiley Online Library on [16/04/2026]. See the Terms and Conditions (https://onlinelibrary.wiley.com/terms-and-conditions) on Wiley Online Library for rules of use; OA articles are governed by the applicable Creative Commons License

Electronics, Electrical Drives, Automation and Motion (SPEEDAM) (2024), 307–312, https://doi.org/10.1109/SPEEDAM61530.2024.10609205.

4. M. M. Belhaouane, M. Ayari, X. Guillaud, and N. B. Braiek, "Robust Control Design of MMC-HVDC Systems Using Multivariable Optimal Guaranteed Cost Approach," *IEEE Transactions on Industry Applications* 55, no. 3 (2019): 2952–2963, https://doi.org/10.1109/TIA.2019.2900606.

5. R. Rosso, J. Cassoli, G. Buticchi, S. Engelken, and M. Liserre, "Robust Stability Analysis of LCL Filter Based Synchronverter Under Different Grid Conditions," *IEEE Transactions on Power Electronics* 34, no. 6 (2019): 5842–5853, https://doi.org/10.1109/TPEL.2018.2867040.

6. K. Zhou and J. C. Doyle, *Essentials of Robust Control*, Vol. 104 (Prentice Hall, 1998).

7. B. Chaudhuri, B. C. Pal, A. C. Zolotas, I. M. Jaimoukha, and T. C. Green, "Mixed-Sensitivity Approach to H_∞ Control of Power System Oscillations Employing Multiple FACTS Devices," in *2003 IEEE Power Engineering Society General Meeting (IEEE Cat. No.03CH37491)* (IEEE, 2003), 2348, https://doi.org/10.1109/PES.2003.1270999.

8. F. Cecati and M. Liserre, "Interoperability Specifications for Multi-Vendor Converter-Dominated Grid: A Robust Stability Perspective," *IEEE Transactions on Smart Grid* 16, no. 4 (2025): 3003–3016, https://doi.org/10.1109/TSG.2025.3555402.

9. D.-W. Gu, P. Petkov, and M. M. Konstantinov, *Robust Control Design With MATLAB®*, 2nd ed. (Springer Science & Business Media, 2013), https://doi.org/10.1007/978-1-4471-4682-7.

10. S. D'Arco, J. A. Suul, and O. B. Fosso, "A Virtual Synchronous Machine Implementation for Distributed Control of Power Converters in Smartgrids," *Electric Power Systems Research* 122 (2015): 180–197, https://doi.org/10.1016/j.epsr.2015.01.001.

11. C. Collados-Rodriguez, M. Cheah-Mane, E. Prieto-Araujo, and O. Gomis-Bellmunt, "Stability Analysis of Systems With High VSC Penetration: Where is the Limit?," *IEEE Transactions on Power Delivery* 35, no. 4 (2020): 2021–2031, https://doi.org/10.1109/TPWRD.2019.2959541.

12. N. Pogaku, M. Prodanovic, and T. C. Green, "Modeling, Analysis and Testing of Autonomous Operation of an Inverter-Based Microgrid," *IEEE Transactions on Power Electronics* 22, no. 2 (2007): 613–625, https://doi.org/10.1109/TPEL.2006.890003.

13. O. Mo, S. D'Arco, and J. A. Suul, "Evaluation of Virtual Synchronous Machines With Dynamic or Quasi-Stationary Machine Models," *IEEE Transactions on Industrial Electronics* 64, no. 7 (2017): 5952–5962, https://doi.org/10.1109/TIE.2016.2638810.

14. S. Skogestad and I. Postlethwaite, *Multivariable Feedback Control: Analysis and Design*, 2nd ed. (Wiley, 2005).

15. F. Milano, I. Dassios, M. Liu, and G. Tzounas, *Eigenvalue Problems in Power Systems* (CRC Press, 2021), https://doi.org/10.1201/9780429325311.

16. L. Huang, H. Xin, and F. Dorfler, "H_∞-Control of Grid-Connected Converters: Design, Objectives and Decentralized Stability Certificates," *IEEE Transactions on Smart Grid* 11, no. 5 (2020): 3805–3816, https://doi.org/10.1109/TSG.2020.2984946.

17. J. Doyle, K. Glover, P. Khargonekar, and B. Francis, "Statespace Solutions to Standard H_2 and H_∞ Control Problems," in *1988 American Control Conference* (IEEE, 1988), 1691–1696, https://doi.org/10.23919/ACC.1988.4789992.

18. International Electrotechnical Commission (IEC), IEC 60909-0: Short-Circuit Currents in Three-Phase AC Systems. Part 0: Calculation of Currents (IET, 2016).

19. J. Freytes, "Small-Signal Stability Analysis of Modular Multilevel Small-Signal Stability Analysis of Modular Multilevel Converters and Application to MMC-Based Multi-Terminal DC Grids" (Ph.D. thesis, Ecole Centrale de Lille, 2017), https://theses.hal.science/tel-01806049v2.

20. Z. Ali, N. Christofides, L. Hadjidemetriou, E. Kyriakides, Y. Yang, and F. Blaabjerg, "Three-Phase Phase-Locked Loop Synchronization Algorithms for Grid-Connected Renewable Energy Systems: A Review," *Renewable and Sustainable Energy Reviews* 90 (2018): 434–452, https://doi.org/10.1016/j.rser.2018.03.086.

21. J. Girona-Badia, J. C. Olives-Camps, V. A. Lacerda, E. Prieto-Araujo, and O. Gomis-Bellmunt, "Control Performance and Stability Analysis of Frequency Estimator in Grid-Forming Synchronization Control," *Journal of Modern Power Systems and Clean Energy* (2025): 1–12, https://doi.org/10.35833/MPCE.2025.000144.

22. O. C. Sakinci, "Modeling of the Modular Multilevel Converter Using Dynamic Phasors: Reduced-Order Models for Small-Signal Stability Analysis" (PhD diss., KU Leuven, 2022).

23. S. Sumsurooah, M. Odavic, and S. Bozhko, "A Modeling Methodology for Robust Stability Analysis of Nonlinear Electrical Power Systems Under Parameter Uncertainties," *IEEE Transactions on Industry Applications* 52, no. 5 (2016): 4416–4425, https://doi.org/10.1109/TIA.2016.2581151.

24. S. Sumsurooah, M. Odavic, and S. V. Bozhko, "Approach to Robust Stability Domains in the Space of Parametric Uncertainties for a Power System With Ideal CPL," *IEEE Transactions on Power Electronics* 33 (2018): 833–844, https://doi.org/10.1109/TPEL.2017.2668900.

25. L. Kong, Y. Xue, L. Qiao, and F. Wang, "Review of Smallsignal Converter-Driven Stability Issues in Power Systems," *IEEE Open Access Journal of Power and Energy* 9 (2022): 29–41, https://doi.org/10.1109/OAJPE.2021.3137468.

Appendix A: System Parameters

Table A.1 reports the system parameters including the AC system Thévenin equivalent and the VSC electrical and control parameters.

TABLE A.1 | System parameters.

Category	Symbols and values			
	ω^*	1 p.u.	ω_b	$2\pi \cdot 50$ rad/s
Thévenin	k	10	V_b	380 kV
	c	1		
VSC				
Base values	S_b	250 MVA	V_b	380 kV
RLC filter	r_f	0.01 p.u.	l_f	0.20 p.u.
	c_f	0.17 p.u.		
Measurement	T_s	0.001 s		
PLL	$K_\mathrm{p,PLL}$	0.28	$K_\mathrm{i,PLL}$	12.6
	$\omega_\mathrm{bw,PLL}$	$2\pi \cdot 10$ rad/s	$\omega_\mathrm{bw,LPF}$	$2\pi \cdot 75$ rad/s
	$v_\mathrm{o,p}^\mathrm{q*}$	0		
VSM	H	4 s	K_d	100
	K_ω	5	p_AC^*	0.5 p.u.
Q droop	$K_{\mathrm{q}_\mathrm{AC}}$	0.20	q_AC^*	0 p.u.
	$v_\mathrm{c}^\mathrm{d*}$	1 p.u.		
QSEM	ω_vf	200 rad/s	r_s	0 p.u.
	l_s	0.25 p.u.	$v_\mathrm{eq,c}^\mathrm{q*}$	0
Current control	$K_\mathrm{p,cc}$	0.83	$K_\mathrm{i,cc}$	565.5
	$\omega_\mathrm{bw,cc}$	$2\pi \cdot 150$ rad/s		

17518695, 2026, 1, Downloaded from https://ietresearch.onlinelibrary.wiley.com/doi/10.1049/gtd2.70291 by Technische Universität Hamburg Universitätsbibliothek, Wiley Online Library on [16/04/2026]. See the Terms and Conditions (https://onlinelibrary.wiley.com/terms-and-conditions) on Wiley Online Library for rules of use; OA articles are governed by the applicable Creative Commons License

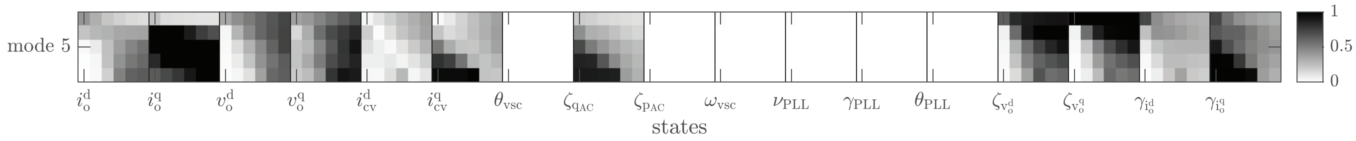

FIGURE A.1 | Participation factors for mode 5 depending on the SCR and the bandwidth ω_{vf}. The explanation for reading the diagram is given in Figure A.4.

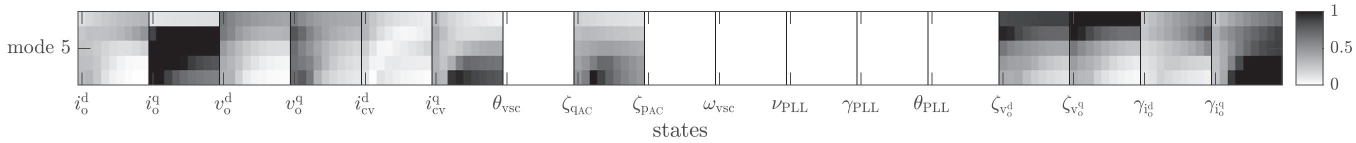

FIGURE A.2 | Participation factors for mode 5 depending on the SCR and the virtual inductance l_s.

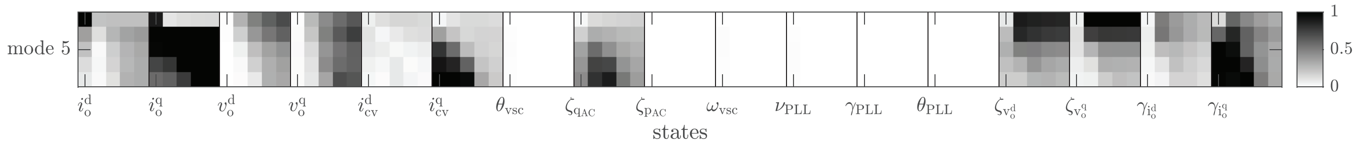

FIGURE A.3 | Participation factors for mode 5 depending on the SCR and the current control bandwidth $\omega_{bw,cc}$.

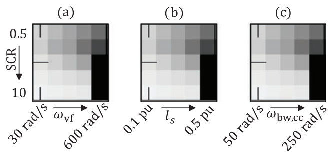

FIGURE A.4 | Explanation on how to read the participation factor diagrams. (a) Corresponds to Figure A.1, (b) to Figure A.2, and (c) to Figure A.3.

Appendix B: Algebraic Equations for Parameter-Dependent Operating Point Determination

With given $\boldsymbol{v}_{\mathbf{o}}^{\mathbf{dq}}(p_1, p_2)$, thus given $\underline{v}_{o}(p_1, p_2)$, and Equation (26), $\underline{i}_{o}(p_1, p_2)$ and $\underline{i}_{cv}(p_1, p_2)$ can be calculated. Taken together with the system equations, this results in the system states (21) at the operating point $\boldsymbol{x}_0$:

$$\boldsymbol{i}_{\mathbf{o,0}}^{\mathbf{dq}}(p_1, p_2) = \left[\mathcal{Re}\left\{\underline{i}_{o}(p_1, p_2)\right\}, -\mathcal{Im}\left\{\underline{i}_{o}(p_1, p_2)\right\}\right]^{\mathsf{T}}, \tag{B.1a}$$

$$\boldsymbol{i}_{\mathbf{cv,0}}^{\mathbf{dq}}(p_1, p_2) = \left[\mathcal{Re}\left\{\underline{i}_{cv}(p_1, p_2)\right\}, -\mathcal{Im}\left\{\underline{i}_{cv}(p_1, p_2)\right\}\right]^{\mathsf{T}}, \tag{B.1b}$$

$$\Delta\theta_{vsc,0}(p_1, p_2) = -\arctan\left(\frac{e_0^q(p_1, p_2)}{e_0^d(p_1, p_2)}\right), \tag{B.1c}$$

$$\zeta_{qAC,0}(p_1, p_2) = \mathcal{Im}\left\{\underline{s}_{o}(p_1, p_2)\right\}, \tag{B.1d}$$

$$\zeta_{PAC,0}(p_1, p_2) = p_{AC}^{*}, \tag{B.1e}$$

$$\omega_{vsc,0}(p_1, p_2) = 1, \tag{B.1f}$$

$$\nu_{PLL,0}(p_1, p_2) = 0, \tag{B.1g}$$

$$\gamma_{PLL,0}(p_1, p_2) = 1, \tag{B.1h}$$

$$\Delta\theta_{PLL,0}(p_1, p_2) = -\arctan\left(\frac{v_{o,0}^q(p_1, p_2)}{v_{o,0}^d(p_1, p_2)}\right), \tag{B.1i}$$

$$\begin{aligned}\boldsymbol{\zeta}_{v_o^{dq},0}(p_1, p_2) = &\begin{bmatrix}\cos\left(\Delta\theta_{vsc,0}(p_1, p_2)\right) \cdot v_{o,0}^d(p_1, p_2) \\ \sin\left(\Delta\theta_{vsc,0}(p_1, p_2)\right) \cdot v_{o,0}^d(p_1, p_2)\end{bmatrix}\cdots \\ &\begin{bmatrix}-\sin\left(\Delta\theta_{vsc,0}(p_1, p_2)\right) \cdot v_{o,0}^q(p_1, p_2) \\ +\cos\left(\Delta\theta_{vsc,0}(p_1, p_2)\right) \cdot v_{o,0}^q(p_1, p_2)\end{bmatrix},\end{aligned} \tag{B.1j}$$

$$\boldsymbol{\gamma}_{\mathbf{i}_{\mathbf{o}}^{\mathbf{dq}},\mathbf{0}}(p_1, p_2) = \begin{bmatrix}\frac{1}{K_{i_{cc}}} \cdot \left(v_{cv,c,0}^d(p_1, p_2) - l_f \cdot i_{cv,c,0}^q(p_1, p_2)\right) \\ \frac{1}{K_{i_{cc}}} \cdot \left(v_{cv,c,0}^q(p_1, p_2) + l_f \cdot i_{cv,c,0}^d(p_1, p_2)\right)\end{bmatrix}. \tag{B.1k}$$

17518695, 2026, 1, Downloaded from https://ietresearch.onlinelibrary.wiley.com/doi/10.1049/gtd2.70291 by Technische Universität Hamburg Universitätsbibliothek, Wiley Online Library on [16/04/2026]. See the Terms and Conditions (https://onlinelibrary.wiley.com/terms-and-conditions) on Wiley Online Library for rules of use; OA articles are governed by the applicable Creative Commons License